Nano Research

Open Access

Research Article

A multifunctional exudate-absorptive patch accelerates burn wound healing via antioxidant, anti-inflammatory and immunomodulatory effects

Que Bai[1,§], Yuzhu Wang[1,§], Gaopeng Dang[1,§], Jiaxin Hao[1], Yingbo Ji[1], Yu Wei[1], Xufang Liu[1], Yifei Wang[1], Lei Wei[2] ✉, Junting Gu[1] ✉, and Lina Niu[1] ✉

[1] *State Key Laboratory of Oral & Maxillofacial Reconstruction and Regeneration, National Clinical Research Center for Oral Diseases, Shaanxi Key Laboratory of Stomatology, Department of Prosthodontics, School of Stomatology, The Fourth Military Medical University, Xi'an 710032, China*

[2] *School of Electrical and Electronic Engineering, Nanyang Technological University, Singapore 639798, Singapore*

§ *Que Bai, Yuzhu Wang, and Gaopeng Dang contributed equally to this work.*

Cite this article: *Nano Research*, **2026**, *19*, 94908787. https://doi.org/10.26599/NR.2026.94908787

ABSTRACT: Burn wounds present significant challenges for traditional dressings due to excessive exudate secretion and persistent inflammation. To address these, the study developed a multifunctional high-exudate-absorption patch (SPC@C) loaded with bioactive curcumin nanoparticles for enhanced burn wound healing. A biomimetic three-dimensional nanoflower hybrid was synthesized through a mild one-pot self-assembly process. It was loaded into an acrylamide-sodium alginate hydrogel and dried, producing the SPC@C patch. The exudate absorption capacity, drug release characteristics, as well as anti-inflammatory and antioxidant properties of the patch were systematically studied. Additionally, the pro-healing performance and potential mechanisms *in vivo* were evaluated using a rat burn model. SPC@C absorbs wound exudate rapidly, transforming its initially dense internal network to a macroporous structure, thereby facilitating the release of the bioactive curcumin. *In vitro*, SPC@C exhibited a significant capacity to scavenge reactive oxygen species (ROS) and mitigate the loss of mitochondrial membrane potential. Furthermore, it suppressed the expression of pivotal pro-inflammatory cytokines (tumor necrosis factor-*α* and interleukin-1*β*) and modulated macrophage M1-to-M2 polarization. *In vivo*, SPC@C significantly improved epidermal regeneration, angiogenesis, and collagen deposition in burn tissues. RNA sequencing analysis showed that in burn tissues, SPC@C releases curcumin to modulate antioxidant and anti-inflammatory immunomodulation by regulating the AMPK/Sirt3/NF-*κ*B signaling axis. This work provides a theoretical foundation for developing materials aimed at managing burn wound exudate and modulating the immune responses.

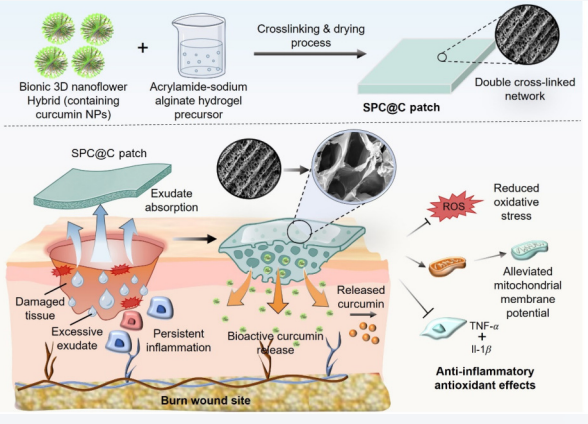

KEYWORDS: exudate absorption, anti-inflammatory, reactive oxygen species (ROS) scavenging, burn healing

1 Introduction

Burns can result from cold, heat, friction, radiation, chemical, or electrical sources in anyone at any time or place [1]. Burn wounds are typically characterized by copious exudate. It leads to complications, such as wound deterioration, infection, persistent inflammation, and even delayed healing process [2–4]. Excessive and prolonged wound exudate has been shown to macerate the peri‑wound skin, degrade key extracellular matrix components, and sustain a pro-inflammatory environment that hinders re‑epithelialization [5]. In clinical practice, an ideal wound dressing should remove timely this excessive exudate effectively. To address this, various hydrophilic wound dressings, such as medical gauze, porous sponges, and gelatin, have been clinically employed for exudate absorption [6–10]. However, these dressings have slow

Received: March 2, 2026; **Revised:** April 27, 2026
Accepted: April 29, 2026

✉Address correspondence to Lina Niu, niulina831013@126.com; Junting Gu, 15094031504@163.com; Lei Wei, wei.lei@ntu.edu.sg

absorption rates and struggle to effectively remove accumulated fluid, contributing to suboptimal healing outcomes [11, 12]. Moreover, traditional dressings often exhibit limited fluid-holding capacity and are prone to leakage or strike-through, which increases the risk of secondary infection and necessitates frequent dressing changes [13]. Furthermore, these dressings lack effective capabilities to modulate the inflammatory response or promote tissue regeneration [14]. Recent advances in exudate-absorptive polymeric patches have demonstrated that rational design, based on hydrophilic polymer networks, microporous architecture, and directional fluid transport, can significantly enhance absorption rate and retention capacity [15–17]. Therefore, developing novel dressings that can manage excessive wound exudate and regulate the wound immune microenvironment potently is of paramount importance.

A defining characteristic of the burn wound microenvironment is its aberrant metabolic activity, marked by disruptions in reactive oxygen species (ROS) and cytokines. This imbalance leads to a disruption of redox homeostasis and creates an inflammatory milieu dominated by excessive ROS [18–20]. Sustained high levels of ROS inhibit the functional shift of macrophages from the pro-inflammatory M1 to the anti-inflammatory M2 phenotype. They also promote the aberrant secretion of pro-inflammatory cytokines, exacerbating the inflammatory cascade [21–23]. Furthermore, prolonged exposure to a ROS-enriched milieu can impair cellular redox balance and mitochondrial functional integrity. This consequently hinders critical repair processes including granulation tissue formation, re-epithelialization, and collagen synthesis [24, 25]. Therefore, it is imperative to develop an integrated intervention system incorporating both ROS-scavenging and anti-inflammatory functionalities to reconstruct a pro-regenerative microenvironment and accelerate wound healing.

Curcumin (Cur), a natural extract from turmeric, functions as both an antioxidant and anti-inflammatory agent, making it a promising candidate for wound treatment [26]. Specifically, it can enhance antioxidant capacity by activating the nuclear factor erythroid 2-related factor 2 (Nrf2) pathway to scavenge ROS [27], and effectively promote the healing process by suppressing the production of key inflammatory factors, including tumor necrosis factor-α (TNF-α) and interleukin-6 (IL-6) [28]. Therefore, drug delivery systems incorporating curcumin have been demonstrated to effectively mitigate excessive inflammation and oxidative stress in wounds [29–31]. However, the inherent drawbacks of curcumin, including poor water solubility, low chemical stability, and a short half-life, limit its bioavailability and ultimate therapeutic efficacy. To address this challenge, this study designed a novel nanoflower structure based on nanodrug delivery theory, aiming to improve the delivery efficiency and therapeutic efficacy of curcumin.

In this study, Cur nanoparticle-loaded nanoflowers were constructed via a one-step self-assembly approach. These nanoflowers were functionally integrated with a high-exudate-absorption patch (SPC@C) to synergistically promote burn wound repair (Scheme 1). SPC@C absorbed wound exudate quickly, triggering a structural transformation from an initially dense network to a large-pore topological architecture, thereby releasing bioactive Cur. *In vitro* experiments confirmed that this system efficiently scavenged excess ROS, maintained mitochondrial membrane potential stability, significantly downregulated expression of pro-inflammatory cytokines, and promoted macrophage phenotypic transition from M1 to M2. In a burn-induced animal model, SPC@C markedly enhanced epidermal regeneration, neovascularization density, and ordered collagen deposition. RNA-seq analysis revealed that its antioxidant and anti-inflammatory immune regulatory mechanism involved the AMPK/Sirt3/NF-κB signaling axis. This work provides a material basis for developing intelligent dressings with dual functionalities of exudate management and immunomodulation.

2 Experimental

2.1 Synthesis of bovine serum albumin (BSA)-Cu@Cur (BC) nanoflowers

To synthesize BC hybrid nanoflowers, 200 μL of 120 mM $CuSO_4$ and 3 mg of Cur were added to 30 mL BSA, and the mixture was gently shaken at 25 °C for 15 h. Centrifugation at 10,000*g* for 10 min was then applied to collect the precipitates, yielding the final product for storage at −20 °C. Drug loading capacity and encapsulation efficiency of BC nanoflowers were determined by ultraviolet–visible (UV–vis) spectroscopy. The morphology of the BC nanoflowers composite was characterized by scanning electron microscopy (SEM) (S-4800, Hitachi, Japan), while its elementals were determined using energy dispersive spectroscopy (EDS). The chemical states of the constituent elements were further analyzed by X-ray photoelectron spectroscopy (XPS) (K-Alpha, Thermo Scientific, USA). The hydrodynamic size distribution of BC nanoflowers was measured using a Malvern Mastersizer 3000+ Ultra (Malvern Mastersizer, UK). The encapsulation efficiency and loading content of Cur in the BC nanoflowers were quantified using a UV–visible spectrophotometer (P7, MAPADA, China).

2.2 Preparation of SPC@C patches

Two types of 2.2% sodium alginate with an M/G ratio of 1:2 (M_W = 100 kDa) and another with M_W = 20–50 kDa (viscosity 15–60 mPa·s) were mixed at a 1:1 ratio. This mixture was combined with an equal volume of 13.5 wt.% acrylamide solution. 4 mL of the resulting mixture was combined sequentially with 30 μL of N,N'-methylenebisacrylamide (MBAA), 3.2 μL of N,N,N',N'-tetramethylethylenediamine (TEMED), 90.4 μL of ammonium persulfate (APS), 76.4 μL of $CaSO_4$, and 4 mg of BC nanoflowers. The solution was injected into a six-well plate mold and crosslinked for 24 h. The resulting hydrogel was air-dried to form patches (designated SPC@C). Prior to use, a mixture of 2% chitosan, 1-ethyl-3-(3-dimethylaminopropyl)carbodiimide (EDC) and N-hydroxysuccinimide (NHS) was rapidly prepared and coated onto SPC@C patches (25 μL/cm^2). The functionalized patch was then applied under gentle compression to tissue surfaces. The internal morphology of patches was analyzed by SEM. The surface chemical bonds of patches were analyzed by Fourier transform infrared spectroscopy (FTIR, Spectrum3, Perkinelmer, USA) with a scanning range of 400–4000 cm^{-1}.

2.3 Scavenging effect of SPC@C on intracellular ROS

RAW264.7 cells were seeded in confocal dishes (NEST Biotechnology, cat. no. 801002) at a density of 3 × 10^5 cells/mL and cultured for 24 h. The culture medium was replaced with complete Dulbecco's modified Eagle medium (DMEM) containing lipopolysaccharide (LPS, 100 ng/mL, Servicebio, China) and SPC@C (diameter: 5 mm, thickness: 2 mm), with the materials placed above the cells (without direct contact). The cells were then incubated for an additional 24 h. After that, the following fluorescent staining was performed.

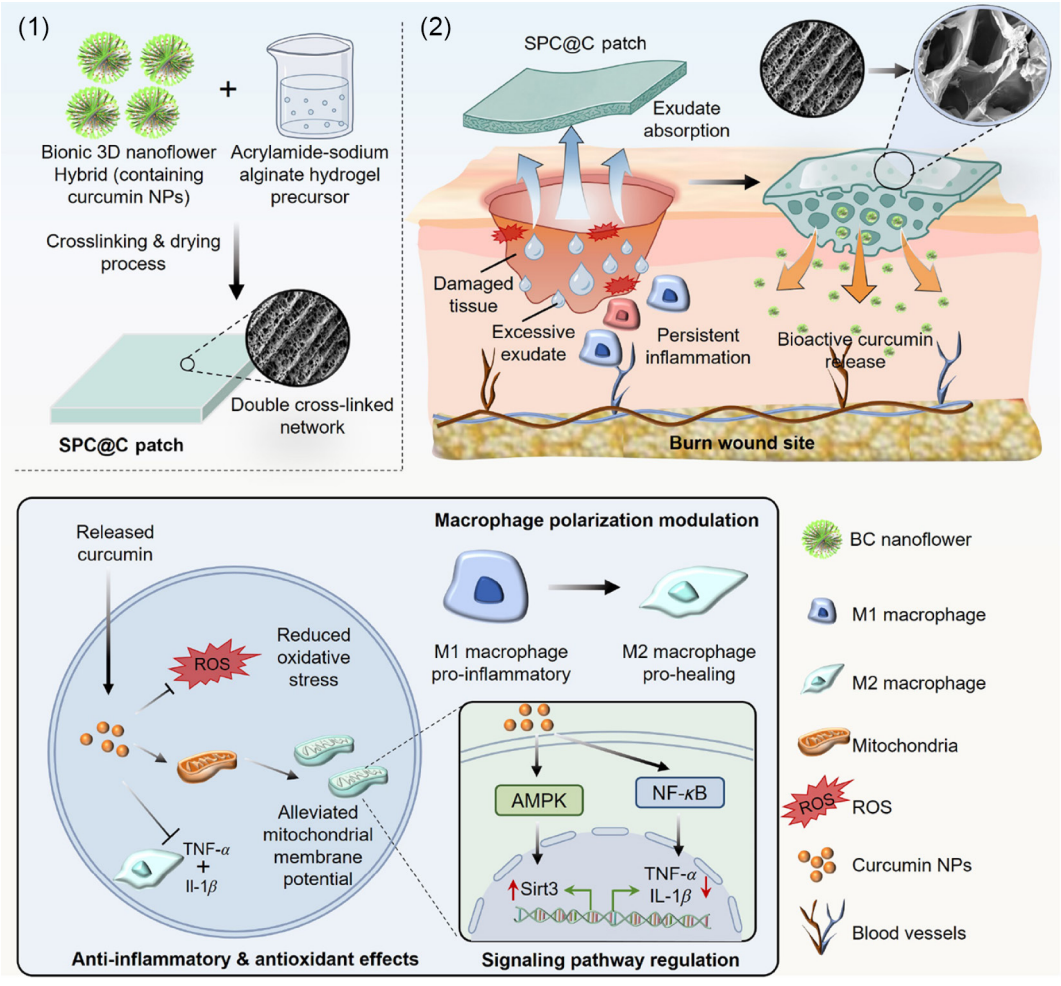

Scheme 1 Schematic illustration of SPC@C patch fabrication and its therapeutic mechanism for accelerated burn healing. (1) Synthetic route of SPC@C patch: BC nanoflower formation, free radical polymerization of acrylamide/sodium alginate network, and calcium ion cross-linking. (2) Multimodal therapeutic mechanism: ROS scavenging via curcumin release, macrophage polarization toward M2 phenotype, and promotion of angiogenesis and collagen deposition.

ROS detection (DCFH-DA method): 2',7'-dichlorodihydrofluorescein diacetate (DCFH-DA) (Elabscience) was diluted with phosphate-buffered saline (PBS) to a final concentration of 10 μM. 1 mL of the diluted solution was added to each dish, and the cells were incubated at 37 °C for 30 min in the dark. After thorough washing, the cells were observed under a laser confocal microscope (Olympus, FV1000, Japan).

Mitochondrial membrane potential assay (JC-1 method): According to the manufacturer's instructions, 1 mL of JC-1 staining working solution (Beyotime) was added to each dish and mixed gently. The cells were incubated in a cell culture incubator at 37 °C for 20 min. The working solution was then aspirated, and the cells were washed twice with JC-1 staining buffer. An appropriate amount of buffer was added to cover the cells, and images were captured using a laser confocal microscope.

To simulate an oxidative stress model, L929 cells (1×10^5 cells/mL) were exposed to 100 μM H_2O_2 in the presence of SPC@C (diameter: 5 mm, thickness: 2 mm) for 24 h. ROS detection and mitochondrial membrane potential analysis were performed identically to RAW264.7 experiments. To detect mitochondrial superoxide generation, we used the MitoSOX™ red probe (MX4313-50UG, Maokang). The final concentration of the probe working solution was 500 nM. Following the manufacturer's instructions, the probe was added to the cells. The cells were incubated at 37 °C for 30 min in the dark. Then, the cells were washed three times with PBS to remove unreacted probe. Finally, fluorescence was observed under a laser confocal microscope and quantified using Image J software.

2.4 Macrophage M1/M2 phenotype polarization assay

RAW264.7 cells were seeded into confocal dishes at a density of 1×10^6 cells/well in 2 mL of complete DMEM and cultured for 24 h. Curcumin (dissolved in dimethyl sulfoxide (DMSO), 10 μM) was used as the positive control. Then, the cells were stimulated with LPS (100 ng/mL) and co-cultured with SPC@C patches (diameter: 5 mm, thickness: 2 mm) for 24 h. After stimulation, the cells were fixed with 4% paraformaldehyde for 15 min at room temperature, and blocked with 5% BSA for 30 min. The cells were then incubated with primary antibodies anti-CD206 (1:600, Proteintech) and anti-CD86 (1:400, Proteintech) for 1 h. After that, the cells were washed three times with PBS. Finally, fluorescence was recorded using a laser confocal microscope and quantified with ImageJ software.

2.5 Animal experiments

All experimental procedures involving animals were reviewed and approved by the Laboratory Animal Ethics Committee of the Air

Force Military Medical University (Approval No: 2024kq-054). Male Sprague-Dawley rats (6-week-old, 150–200 g) were used for all *in vivo* experiments. Anesthesia during the study included 2.5% isoflurane administered via a nose cone, and euthanasia was performed in a carbon dioxide anesthesia resting chamber (YLS-Q14, Jinanyiyan, China). Postoperative analgesia (ibuprofen, Fenbid, Tianjin, China) was administered to the rats in drinking water (200 μg/mL) from 1 h before surgery to 7 days after surgery.

2.6 Establishment of deep burn wound model

Rats were anesthetized via inhalation of 2.5% isoflurane and placed in the prone position. The dorsal hair was removed using an electric clipper followed by depilatory cream, and the exposed skin was disinfected with povidone-iodine. A wax carving pencil (J0806/SJK lab) equipped with a flat circular copper tip (diameter: 10 mm) was employed to create the burn wounds. To ensure consistent wound depth, the probe was brought into contact with the skin without additional manual pressure and maintained at a constant temperature of 200 °C for 10 s. The animals were then randomly assigned to four groups (n = 6 per time point): control group, receiving 0.2 mL of sterile normal saline topically; Cofoe group, treated with Cofoe dressings (10 mm diameter, 2 mm thickness); SPC group, treated with SPC dressings (10 mm diameter, 2 mm thickness); and SPC@C group, treated with SPC@C dressings (10 mm diameter, 2 mm thickness). The initial application was performed immediately post-injury and designated as day 0, and the dressings were subsequently replaced every two days.

2.7 Hematoxylin and eosin (H&E) and Masson's trichrome staining

Animals were euthanized on days 3, 7 and 14, and wound tissues were collected. The tissues were fixed in 4% paraformaldehyde solution for 24 h, followed by dehydration and embedding in paraffin. The tissues were sectioned at an appropriate thickness and soaked in a series of xylene solutions for deparaffinization. Samples were then stained according to standard H&E and Masson staining protocols to evaluate tissue re-epithelialization and collagen deposition. After Masson staining, collagen fibers were dyed blue and the intensity of their expression was quantified by ImageJ software.

2.8 Immunofluorescence staining

Tissue sections underwent antigen retrieval in citrate buffer (pH 6.0, G1202, Servicebio) at 95 °C for 20 min. The sections were blocked with 10% goat serum solution (G1209, Servicebio) for 1 h. The sections were then incubated with primary antibodies overnight at 4 °C at the following dilution ratios: Anti-CD86 (1:200, GB115630, Servicebio), Anti-CD206 (1:500, GB113497, Servicebio), Anti-Sirt3 (1:400, YM8158, Immunoway), Anti-NF-κB p65 (1:450, 10745-1-AP, Proteintech), Anti-CD31 (1:200, GB11063-2, Servicebio), and Anti-Col I (1:1000, GB115707, Servicebio). After washing with PBS, the slides were incubated with the corresponding fluorophore-conjugated antibodies for 2 h, the nuclei were stained with DAPI (G1012, Servicebio), and fluorescence signals were photographed under a confocal laser microscope.

2.9 Statistical analysis

All experimental data are presented as the mean ± standard deviation (SD). All statistical analyses were conducted using GraphPad Prism 8.0 software. Comparisons between groups were performed using the t-test (for two groups) or one-way ANOVA (for three or more groups), followed by Tukey's method for multiple comparisons. The thresholds for statistical significance were defined as $^{*}P < 0.05$, $^{**}P < 0.01$, and $^{***}P < 0.001$.

3 Results and discussion

3.1 Synthesis and characterization of BC nanoflowers

To develop an antioxidant patch, we first prepared antioxidant BSA-Cu@Cur (BC) hybrid nanoflowers. BC hybrid three-dimensional nanoflowers were synthesized via a mild one-pot self-assembly biomimetic process without additional stabilizers. Specifically, a copper sulfate solution was added to bovine serum albumin solution, followed by dropwise addition of Cur dissolved in ethanol (Fig. 1(a)). Coordination between Cu^{2+} and amide groups of the protein scaffold formed complexes, while Cur was loaded into these complexes through self-assembly to create BC nanoflowers. SEM images in Fig. 1(b) revealed the presence of distinct three-dimensional layered structures in the hybrid material, similar to hydrangeas. The stereo stratified structure enhanced the specific surface area of the nanoflowers, enabling them to hold larger amounts of Cur. Energy dispersive spectroscopy (EDS) confirmed homogeneous distribution of Cu, C, O, and N elements throughout the particle matrix (Fig. 1(c)).

During nanoflower growth, the protein template induced copper sulfate formation to construct petal-like scaffolds, coalescing from the periphery toward the center (Fig. 1(d)). BSA-Cu and BC nanoflowers exhibited distinct color transitions from blue to orange-yellow upon aqueous dispersion (Fig. 1(e)). Figure 1(f) shows that upon the addition of curcumin during the synthesis process, BSA induces the formation of a nanoflower scaffold, while curcumin self-assembles into nanoparticles and distributes on the scaffold surface. The preparation of curcumin-loaded nanoflowers was optimized by adjusting the addition ratio of BSA. The copper ion concentration was maintained constant, while variations in the BSA concentration led to the formation of BC nanoflowers with distinct morphologies. At a BSA concentration of 0.1 mg/mL, the resulting BC nanoflowers exhibited a pore size favorable for both drug loading and release. Consequently, this concentration was selected for the synthesis of BC nanoflowers in all subsequent experiments (Fig. S1 in the in the Electronic Supplementary Material (ESM)). Under these conditions, BC nanoflowers exhibited negative surface charge (−22.8 ± 0.81 mV) with an average hydrodynamic diameter of 3.8 ± 0.02 μm (Fig. S2 in the ESM). These flower-like scaffolds were assembled from nanoscale building blocks, and their surfaces were further loaded with curcumin nanoparticles of approximately 26.8 nm in size. As shown in Fig. 1(g) (UV–Vis) and Fig. S3 in the ESM (FTIR), BC nanoflowers exhibited similar characteristic peaks to Cur [32]. X-ray photoelectron spectroscopy (XPS) analysis of BC (Fig. 1(h)) confirmed the presence of Cu, C, O, and N elements, thereby validating EDS results and confirming successful synthesis. In the high-resolution Cu 2p spectrum of BC (Fig. 1(i)), characteristic peaks at 935 and 955 eV represent the Cu $2p_{3/2}$ and Cu $2p_{1/2}$ orbitals, respectively. Furthermore, the drug loading capacity of Cur was estimated at 17.27% ± 0.91%, and the encapsulation efficiency of the nanoparticles reached 54.89% ± 2.05%. Overall, these results demonstrate the successful fabrication of curcumin-loaded BC nanoflowers with favorable structural

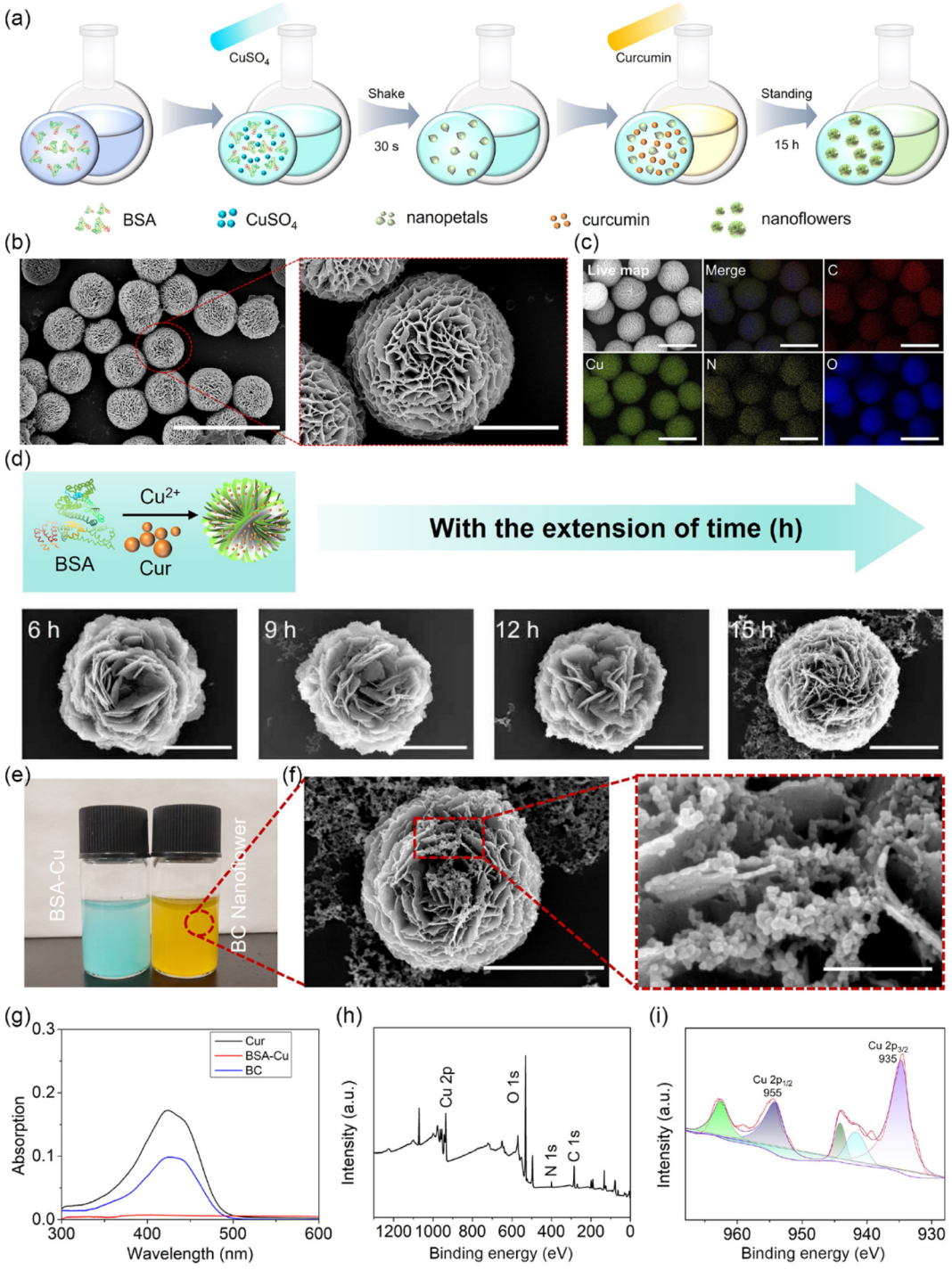

Figure 1 Synthesis and characterization of BC nanoflowers. (a) Schematic diagram of the synthesis of BC nanoflowers. (b) Representative SEM images of BSA-Cu nanoflowers. Scale bar: 10 μm (left panel), 2 μm (right panel). (c) EDS elemental mapping of BC nanoflowers showing distributions of Cu (green), C (red), O (blue), and N (yellow). Scale bars: 5 μm. (d) Time-dependent SEM images documenting morphological evolution during the synthesis of BC nanoflowers. Scale bars: 2 μm. (e) Digital photographs of aqueous dispersions: BSA-Cu nanoflowers (left) and BC nanoflowers (right). (f) SEM images of BC nanoflowers. Scale bar: 2 μm (left panel), 300 nm (right panel). (g) UV–vis absorption spectra of free Cur, BSA-Cu, and BC nanoflowers. (h) XPS survey spectrum of BC nanoflowers. (i) High-resolution Cu 2p XPS spectrum of BC nanoflowers.

features and drug loading properties, establishing a robust foundation for their subsequent application in burn wound management.

3.2 Synthesis and mechanical properties of patches

In this study, a polyacrylamide (PAM)-alginate composite patch (SPC) with energy dissipation properties was integrated with a positively charged polymer adhesive (chitosan). The SPC patch was surface-engineered via 1-ethyl-3-(3-dimethylaminopropyl)carbodiimide/N-hydroxysuccinimide (EDC/NHS) coupling chemistry to integrate chitosan as a bridging network. This mechanism effectively enhanced the adhesion of the

SPC patch to tissues. The synthesized hydrogel was dehydrated and dried to form the SPC patch (Fig. 2(a)). SEM images revealed a loosely porous microstructure in the cross-section of the hydrated SPC (Fig. S4 in the ESM). Upon drying, pore size decreased significantly while density increased (Fig. 2(b)). Persistent wound exudate is a major factor contributing to delayed burn healing [33]. Consequently, the fluid absorption of SPC in liquid was evaluated. Water contact angle indicated that SPC exhibited hydrophilic properties (water contact angle ~ 64.4° ± 0.25°) (Fig. 2(d)). The liquid absorption in deionized water showed that upon contact with liquid, the SPC pores swelled rapidly, forming an expanded porous structure (Fig. 2(c)). Pore size further increased progressively with absorption time (Fig. 2(e)). SPC demonstrated exceptional water absorption, achieving a rate of 1275% ± 16.59% within 24 h, substantially higher than commercial hydrocolloids (Cofoe) (56% ± 1.23%) (Fig. 2(f)). The material adheres to the polar groups (e.g., –COOH, $–NH_2$) on the skin surface through hydrogen bonding and electrostatic interactions. Upon absorption of wound exudate, the polymer network of the hydrogel is progressively expanded, resulting in a looser structure that allows the material, originally tightly adhered to the tissue, to be easily detached (Fig. 2(h)). This sustained absorption capability confirms the potential of the SPC@C patch for effectively managing persistent wound exudate. This hydration-induced softening correlates with hydrogel network expansion observed via SEM. We further evaluated the *in vitro* Cur release from the SPC@C patch. As illustrated in Fig. 2(g), Cur exhibited a burst release during the initial 12 h (58.2% ± 3.1%), followed by gradual deceleration after 24 h. These results demonstrate that the Cur loaded in the patch possesses sustained-release characteristics, which is beneficial for prolonged therapeutic efficacy.

Oscillatory frequency and shear strain sweep tests were

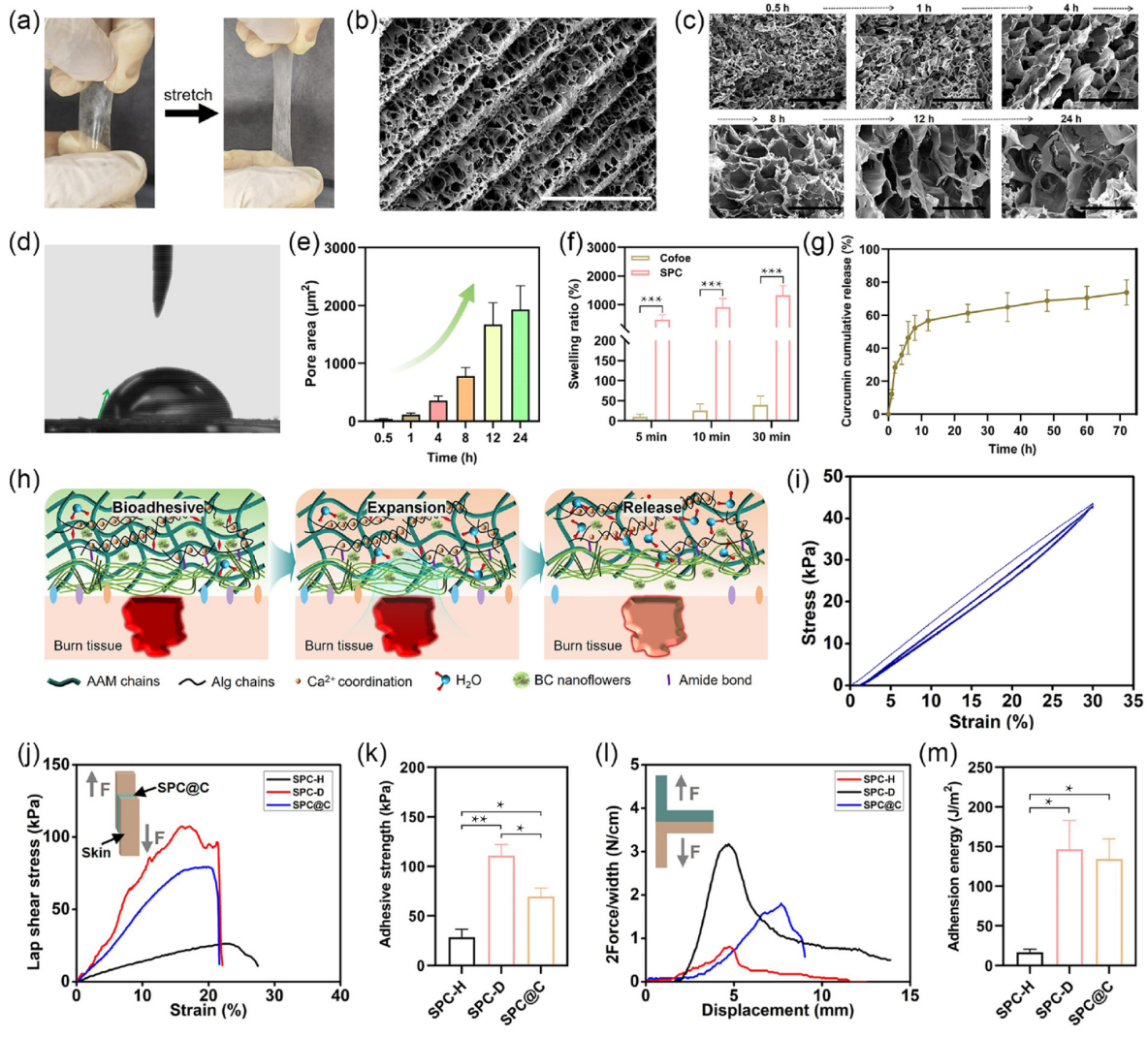

Figure 2 Fabrication and physicochemical characterization of SPC hydrogel patches. (a) Digital photograph and macroscopic morphology of SPC patches. (b) Surface microstructure analyzed by SEM. Scale bar: 500 μm. (c) Time-dependent SEM images of SPC patches after immersion in deionized water. Scale bars: 100 μm. (d) Water contact angle (WCA) measurements. (e) Pore size distribution following hydration (n = 8). (f) The liquid absorption rate of SPC patches (n = 8). (g) Curcumin release from SPC@C patches (n = 10). (h) Schematic illustrating exudate absorption mechanism in burn wounds. (i) Loading-unloading tensile tests at a strain of 30% for 10 cycles without interval. (j) Lap shear stress-strain curve of the material on porcine skin; inset shows a representative image of the lap shear test. (k) Bar chart summarizing the lap shear strength of the material on porcine skin (n = 3). (l) Force-displacement curve of the interfacial toughness between the material and porcine skin under a 180° peel force; inset shows a representative image of the 180° peel test. (m) Interfacial toughness between the material and porcine skin (n = 3). Data was presented as mean ± SD. Statistical analysis was performed by one-way ANOVA. *P < 0.05, **P < 0.01, ***P < 0.001.

conducted to characterize the hydrogels. Within the tested frequency range, the storage modulus of all samples was higher than the loss modulus, and the SPC-D hydrogel exhibited slightly enhanced stiffness (Fig. S5(a) in the ESM). Strain sweep results revealed that all hydrogels displayed linear viscoelasticity under low shear strain (γ = 0.1%–10%). At large strains, the materials transitioned to a fluid-like state, accompanied by a slight peak in loss modulus (Fig. S5(b) in the ESM), which demonstrates the energy dissipation capacity of the hydrogels. The energy dissipation and structural coordination abilities of SPC@C patches were analyzed through cyclic loading-unloading tensile tests. The SPC@C hydrogel exhibited a dissipated energy of ~ 2.95 kJ/m^3 after 10 consecutive tensile cycles (Fig. 2(i)), which is comparable to or higher than many reported soft hydrogels under similar test conditions. This moderate yet effective energy dissipation capacity enables the patch to withstand repeated mechanical deformation without catastrophic failure, making it suitable for dynamic tissue environments.

Furthermore, the adhesion strength of the materials to porcine skin before and after water absorption was analyzed [34, 35]. Porcine skin was chosen as the substrate based on its structural and functional similarities to human skin [36, 37]. The lap shear test results showed that SPC@C exhibited an adhesion strength of 70 ± 4.34 kPa, which was lower than that of SPC-D (111 ± 5.39 kPa) but higher than that of SPC-H (28.5 ± 4.07 kPa) (Figs. 2(j) and 2(k)). Effective tissue adhesion is a fundamental requirement for functional wound dressings. Excessive adhesion strength can complicate dressing removal and damage tissue during replacement [38]. Previous studies indicate that an optimal tissue adhesion range of 45–180 J/m^2 is suitable for wound management [39, 40], ensuring secure fixation while preventing trauma from over-adhesion. Subsequently, a 180° peel test was performed to investigate the influence of material surfaces on the adhesion strength to porcine skin, as shown in Figs. 2(l) and 2(m). The SPC-D material surface exhibited an interfacial toughness of 147 ± 6.22 J/m^2 (higher than that of SPC-H under hydrated conditions, 16 ± 1.18 J/m^2), while the interfacial toughness of SPC@C was slightly lower, at 134 ± 5.24 J/m^2, indicating that the materials can effectively adhere to tissue.

3.3 Oxidative stress protection by SPC@C

To develop a multifunctional wound dressing with controlled drug release and redox modulation capabilities, we engineered a composite system (SPC@C). This composite structure can continuously release Cur and exert its antioxidant function. Before evaluating its wound-healing efficacy *in vivo*, we comprehensively assessed its biocompatibility and migration properties *in vitro*. Results demonstrated favorable cell viability in the SPC@C group (Figs. S6(a)–S6(c) in the ESM), with no significant apoptosis detected after 48 h of culture. Furthermore, scratch assays confirmed that SPC@C significantly enhanced cell migration compared to the control group (Figs. S7(a) and S7(b) in the ESM).

Excessive accumulation of ROS in burn wounds causes oxidative damage to surrounding cells and tissues [41]. Moreover, persistently elevated ROS levels increased pro-inflammatory cytokines secretion, establishing a vicious cycle of inflammation that exacerbates tissue damage and impedes wound healing [42, 43]. Consequently, scavenging elevated ROS levels is crucial for restoring cellular function and facilitating tissue regeneration. This study evaluated the protective effects of SPC@C against oxidative stress using H_2O_2-stimulated L929 cells. As shown in Fig. 3(a), H_2O_2 treatment significantly increased intracellular fluorescence intensity, indicating elevated ROS levels. In contrast, SPC@C markedly reduced ROS-associated fluorescence intensity. Quantified dichlorofluorescein (DCF) fluorescence intensity (Fig. 3(b)) and three-dimensional surface plots visualizing spatial ROS distribution (Fig. 3(c)) collectively confirmed the ROS scavenging capability of SPC@C. Furthermore, we assessed the intracellular antioxidant defense system, specifically superoxide dismutase (SOD) and catalase [44, 45]. qPCR analysis revealed that SPC@C significantly upregulated mRNA expression of both catalase (CAT) and superoxide dismutase 2 (SOD2) (Figs. 3(g) and 3(h)). SPC@C demonstrated significant cytoprotective effects against H_2O_2-induced oxidative stress by effectively scavenging ROS and enhancing endogenous antioxidant defenses (upregulating SOD/CAT expression).

Mitochondria serve as a primary site for the generation of ROS [46]. Mitochondrial membrane potential (MMP) stability is a crucial indicator for assessing mitochondrial status [47]. A decrease in MMP is characterized by increased green fluorescence intensity, which indicates mitochondrial dysfunction. In this study, H_2O_2-stimulated cells showed enhanced green fluorescence derived from J-monomer, suggesting excessive ROS accumulation and mitochondrial dysfunction. By contrast, the SPC@C patch effectively downregulated the green fluorescence intensity and regulated the transition of J-monomer/J-aggregate, thereby alleviating oxidative mitochondrial damage (Figs. 3(d) and 3(e)). Further Image J analysis revealed a significantly lower red/green fluorescence ratio in the H_2O_2-treated group compared to the control group. SPC@C effectively increased this ratio (Fig. 3(f)), demonstrating that it inhibited the H_2O_2-induced MMP decline in L929. MitoSOX Red, a specific mitochondrial superoxide indicator, was used to detect mitochondrial superoxide levels within cells [48]. Following SPC@C treatment, mitochondrial superoxide production was significantly reduced (Figs. 3(i) and 3(j)). Collectively, these results demonstrate that SPC@C exhibits ROS-scavenging activity, restores impaired endogenous antioxidant defenses, and mitigates oxidative mitochondrial damage by eliminating mitochondrial superoxide and recovering MMP.

3.4 The anti-inflammatory effect of SPC@C

Macrophages can polarize into distinct functional phenotypes in response to different microenvironmental cues, primarily the classically activated (M1) and alternatively activated (M2) subtypes [49]. M1 macrophages promote inflammation, whereas M2 macrophages are involved in immune regulation and tissue remodeling [50]. Upon inflammatory stimulation, macrophages can undergo a dysregulation in the balance between their pro-inflammatory and anti-inflammatory functions. This dysregulation exacerbates ROS generation and sustains a pro-inflammatory microenvironment, which subsequently impedes the wound healing process [51]. Therefore, we employed qPCR analysis to evaluate the anti-inflammatory capacity of SPC@C after co-incubation with macrophages. Expression of inflammation-related genes was assessed in macrophages stimulated with LPS (Fig. 4(a)). The significant upregulation of TNF-α and IL-1β mRNA following 24 h of LPS treatment, as shown in Figs. 4(b) and 4(c), confirmed the successful polarization of macrophages toward a pro-inflammatory M1 phenotype. In contrast, SPC@C treatment effectively suppressed these pro-inflammatory genes

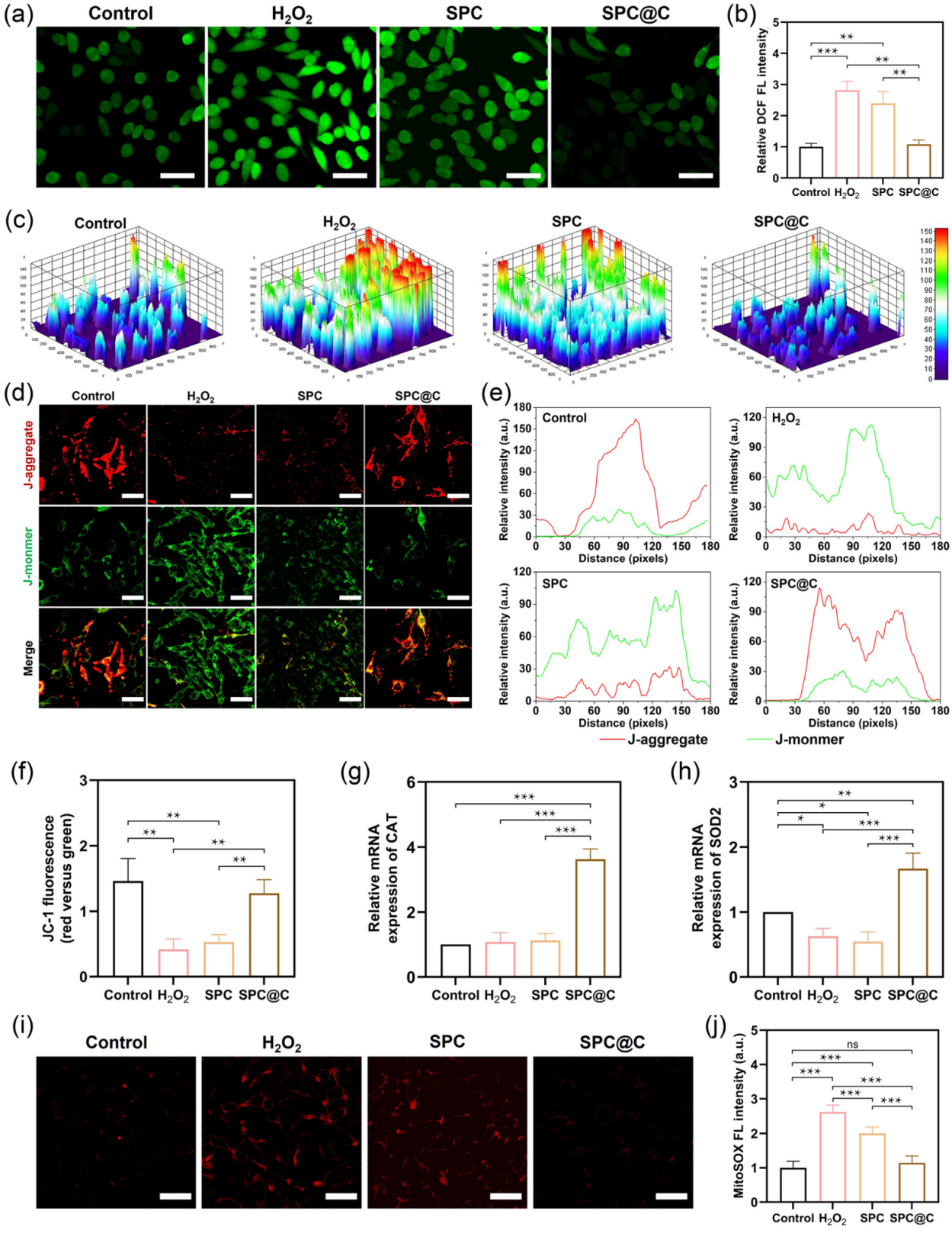

Figure 3 SPC@C-mediated ROS scavenging and oxidative stress mitigation. (a) Representative confocal images of intracellular ROS in L929 fibroblasts under H_2O_2 stimulation detected by DCFH-DA. Scale bars: 40 μm. (b) Quantified DCF fluorescence intensity (n = 3). (c) Three-dimensional surface plots visualize spatial ROS distribution. (d) The mitochondrial membrane potential ($\Delta\Psi_m$) was determined by JC-1 staining. JC-1 forms J-aggregates (red fluorescence) in mitochondria with high $\Delta\Psi$m, whereas it exists as J-monomers (green fluorescence) when $\Delta\Psi_m$ is low. Scale bars: 40 μm. (e) Co-localization analysis of $\Delta\Psi_m$ (red: J-aggregates; green: J-monomers). (f) JC-1 aggregate-to-monomer fluorescence intensity ratio (n = 3). Relative mRNA expression of (g) CAT and (h) SOD2 post-H_2O_2 challenge (n = 3). (i) Mitochondrial superoxide detection using MitoSOX™ Red. Scale bars: 40 μm. (j) Quantified MitoSOX™ fluorescence intensity (n = 3). Data was presented as mean ± SD. Statistical analysis was performed by one-way ANOVA. ns, no significance; *P < 0.05, **P < 0.01, and ***P < 0.001.

while concurrently elevating the expression of the anti-inflammatory markers IL-10 and Arg-1 (Figs. 4(d) and 4(e)). Immunofluorescence staining revealed that in LPS-stimulated macrophages, SPC@C simultaneously downregulated CD86 and upregulated CD206 expression (Figs. 4(f)–4(i)), showing a similar trend to the control group. Collectively, these results indicate that the control group represents a physiologically quiescent, non-inflammatory state. Importantly, SPC@C not only reversed LPS-induced M1-type inflammation but also actively polarized macrophages toward an anti-inflammatory M2-like phenotype that exceeds the basal state. The comparable immunofluorescence trends between the control and SPC@C-treated groups suggest restoration of a homeostatic anti-inflammatory state, whereas the qPCR data confirm that SPC@C does not merely maintain the basal state but actively promotes M2 polarization.

ROS act as a key mediator governing the activation of

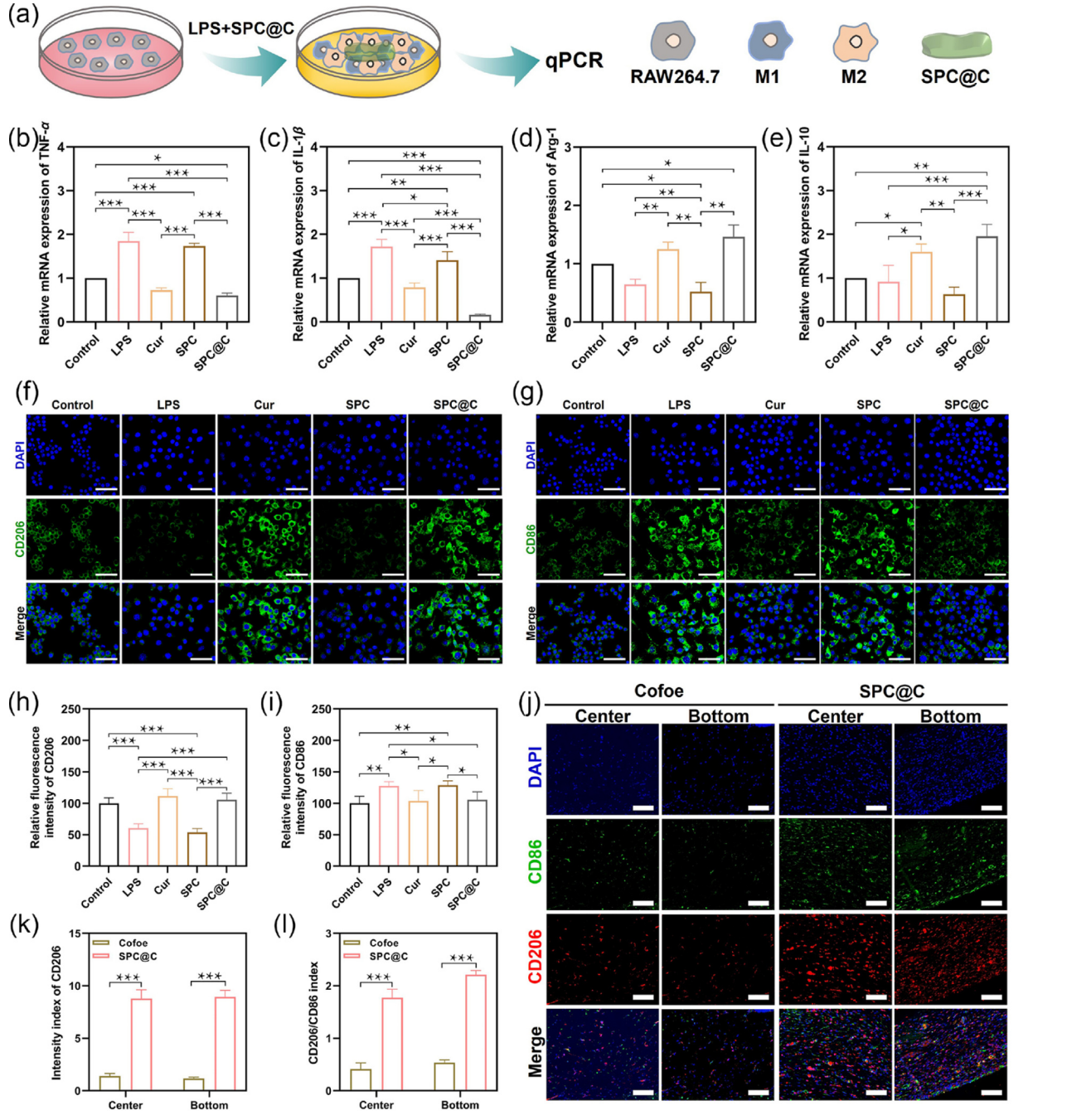

Figure 4 SPC@C patches promote M1-to-M2 macrophage polarization. (a) Schematic mechanism of SPC@C-mediated anti-inflammatory effects in LPS-stimulated macrophages. Relative mRNA expression of (b) TNF-α, (c) IL-1β, (d) Arg-1, and (e) IL-10 in RAW264.7 macrophages after LPS treatment (n = 3). (f) Immunofluorescence staining of CD206 (M2 marker) in treated macrophages. Scale bars: 50 μm. (g) Immunofluorescence staining of CD86 (M1 marker) in treated macrophages. Scale bars: 50 μm. Quantified fluorescence intensity of (h) CD206 and (i) CD86 (n = 4). (j) Dual-immunofluorescence of CD206 (red) and CD86 (green) in macrophages in the wound beds of SPC@C-treated Sprague-Dawley rats. Scale bars: 100 μm. (k) CD206 fluorescence intensity index (n = 3). (l) CD206/CD68 cell ratio quantification (n = 3). Data was presented as mean ± SD. Statistical analysis was performed by one-way ANOVA. ns, no significance; *P < 0.05, **P < 0.01, and ***P < 0.001.

inflammatory signaling pathways within macrophages [52, 53]. To assess the impact of SPC@C on intracellular ROS, we employed confocal laser scanning microscope in LPS-stimulated macrophages. As depicted in Fig. S8 in the ESM, LPS markedly enhanced the intracellular ROS. Notably, cells treated with SPC@C significantly attenuated this fluorescence. Further evaluation of MMP in macrophages revealed that LPS-treated cells exhibited increased green fluorescence and decreased red fluorescence. However, SPC@C effectively ameliorated these alterations (Fig. S9 in the ESM). These results indicate that SPC@C alleviates inflammation by mitigating excessive ROS accumulation and restoring MMP in macrophages under inflammatory conditions. Additionally, rat subcutaneous implantation revealed abundant CD206-positive macrophages around the implant site in the SPC@C group, as compared with the control group (Fig. 4(j)). Meanwhile, the CD206/CD86 ratio was also increased (Figs. 4(k) and 4(l)), indicating enhanced polarization of M2 macrophage phenotypes in the local microenvironment. During the early stage of tissue repair, appropriate activation of M1 macrophages is essential for clearing inflammatory mediators, removing necrotic tissue and foreign debris, and initiating a normal inflammatory response. The upregulation of CD206, in turn, reflects a timely shift of macrophages toward the pro-regenerative M2 phenotype, which supports cell proliferation, matrix deposition, and tissue remodeling. The simultaneous elevation of both markers does not indicate an aberrant pro-inflammatory status, but rather a balanced and sequential immune microenvironment characterized by moderate initial inflammation followed by efficient reparative polarization. Collectively, these results demonstrate that the SPC@C patch elicits moderate M1 activation to initiate normal host defense and tissue clearance, while effectively promoting M2 polarization to facilitate tissue repair.

3.5 Therapeutic effects of SPC@C on skin regeneration

To evaluate the therapeutic effects of SPC@C patch on wound healing, a full-thickness rat burn model (diameter: 10 mm) was created (Fig. 5(a)). Macroscopic observations were conducted at days 0, 3, 7, and 14. Representative images revealed a markedly accelerated rate of wound closure in all treatment groups relative to the control (Figs. 5(b) and 5(c)). Calculation of the wound healing rate revealed that the SPC patch alone enhanced the wound healing rate by 9.73% ± 1.34% compared to the control group, while the SPC@C-treated group enhanced the wound healing rate by 28.69% ± 0.66% (Fig. 5(d)). To further evaluate the effects of SPC@C on burn healing, histological analyses were performed via H&E and Masson's staining (Figs. 5(e) and 5(f)). On day 7, the control group remained a large wound with intense inflammatory responses. In contrast, the SPC@C-treated wound was significantly reduced in size, with alleviated inflammatory infiltration and wound edges contracting toward the center (Fig. 5(g)). On day 14, all patch-treated wounds displayed more pronounced re-epithelialization and changes in skin thickness compared with control group (Fig. 5(i)). Notably, the SPC@C group achieved the highest level of re-epithelialization (approaching the morphology of normal skin) along with a significant reduction in skin thickness (Fig. 5(h)). This reduction in thickness indicates that SPC@C accelerates the transition from proliferative granulation tissue to mature collagen deposition, thereby promoting epidermal maturation.

High-magnification histological images revealed that the control group had limited granulation tissue formation accompanied by extensive inflammatory cell infiltration. In contrast, SPC@C-treated wounds showed almost complete resolution of inflammation, with abundant collagen deposition and the formation of new hair follicles (Fig. 5(f)). Quantitative analysis demonstrated that collagen fibers in the SPC@C group were well-arranged, with a content 2.2-fold higher than that of the control (Fig. 5(j)). In summary, histological results confirm that the SPC@C patch accelerates burn wound healing by effectively reducing tissue inflammation, promoting re-epithelialization, and enhancing structural collagen deposition.

3.6 The transcriptomic analysis of burn wounds

To investigate the underlying mechanistic of SPC@C patch-mediated burn healing, we conducted transcriptomic analysis of skin wound tissues on day 7 post-treatment. Comparative analysis revealed 932 differentially expressed genes (DEGs) between SPC@C-treated and control group, with 804 upregulated and 128 downregulated DEGs (Fig. 6(a)). The heatmap analysis of DEGs demonstrated statistically significant differences between the two groups (Fig. 6(b)). These indicated that the SPC@C patch significantly affected gene expression in burn tissues. Gene Ontology (GO) analysis revealed that downregulated biological processes were predominantly associated with immune cell migration and immune responses (Fig. S10(a) in the ESM). Conversely, upregulated GO terms primarily involved metal ion binding, ion transmembrane transport, and metabolic processes (Fig. S10(b) in the ESM). Kyoto Encyclopedia of Genes and Genomes (KEGG) pathway enrichment analysis demonstrated significant downregulation of inflammation-related pathways in SPC@C-treated wounds, including Cytokine-cytokine receptor interaction, TNF signaling pathway, NF-κB signaling pathway, and IL-17 signaling pathway (Fig. S11(a) in the ESM). This attenuation of excessive inflammation mitigates tissue damage and establishes a pro-repair microenvironment characterized by reduced inflammatory activity. Furthermore, SPC@C treatment upregulated pathways governing: metabolic processes, signal transduction (calcium signaling pathway, AMPK signaling pathway, and peroxisome proliferator-activated receptor (PPAR) signaling pathway), and structural remodeling (extracellular matrix (ECM) receptor–receptor interactions) (Figs. 6(c)–6(e)). These changes enhance energy supply and tissue reconstruction, promoting the transition from the inflammatory to proliferative phase. Consistent with these findings, Gene Set Enrichment Analysis (GSEA) revealed significant positive enrichment of genes related to the AMPK signaling pathway and nicotinamide adenine dinucleotide (NAD) binding (Fig. S11(b) in the ESM). AMP-activated protein kinase (AMPK) activation enhances the expression and activity of its downstream target Sirt3 [54]. Immunofluorescence analysis confirmed increased Sirt3 expression and reduced NF-κB activation (Figs. 6(f)–6(i)), validating functional activation of the AMPK-Sirt3-NF-κB axis in treated wounds. Specifically, AMPK activation enhanced energy supply and antioxidant activity by improving mitochondrial function through Sirt3. It alleviated inflammatory responses by inhibiting NF-κB, thereby creating a favorable environment for tissue repair. Collectively, these transcriptomic findings systematically elucidate the dual mechanism of SPC@C patches. They both mitigate excessive inflammatory responses and promote tissue repair processes.

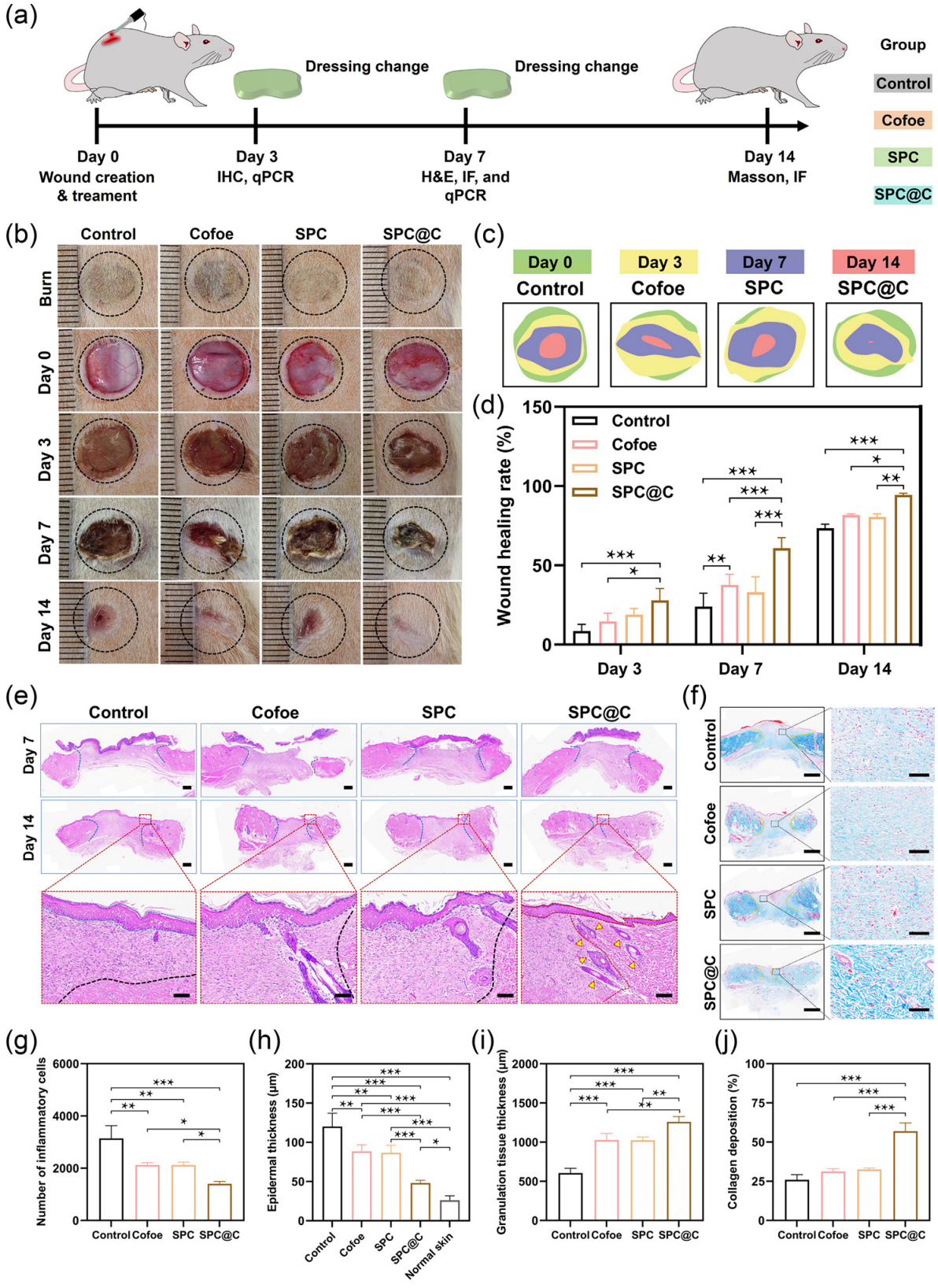

Figure 5 Therapeutic efficacy of SPC@C patches in rat burn healing. (a) Experimental timeline of dorsal burn wound interventions. (b) Representative images of wound closure. (c) Wound margin tracings at days 0, 3, 7, and 14 post-injury. (d) Quantified wound healing rates (n = 4). (e) H&E-stained sections showing epidermal regeneration and granulation tissue formation. Scale bars: 1 mm (small images), 200 μm (magnified images). (f) Histological analysis of collagen deposition (blue) detected by Masson's trichrome staining at day 14. Scale bars: 2 mm (left panel), 200 μm (right panel). Quantitative analysis of the number of (g) inflammatory cells, (h) the epidermal thickness, (i) granulation tissue thickness, and (j) collagen deposition (n = 3). Data was presented as mean ± SD. Statistical analysis was performed by one-way ANOVA. Tukey's method for multiple comparisons. ns, no significance; $^{*}P < 0.05$, $^{**}P < 0.01$, and $^{***}P < 0.001$.

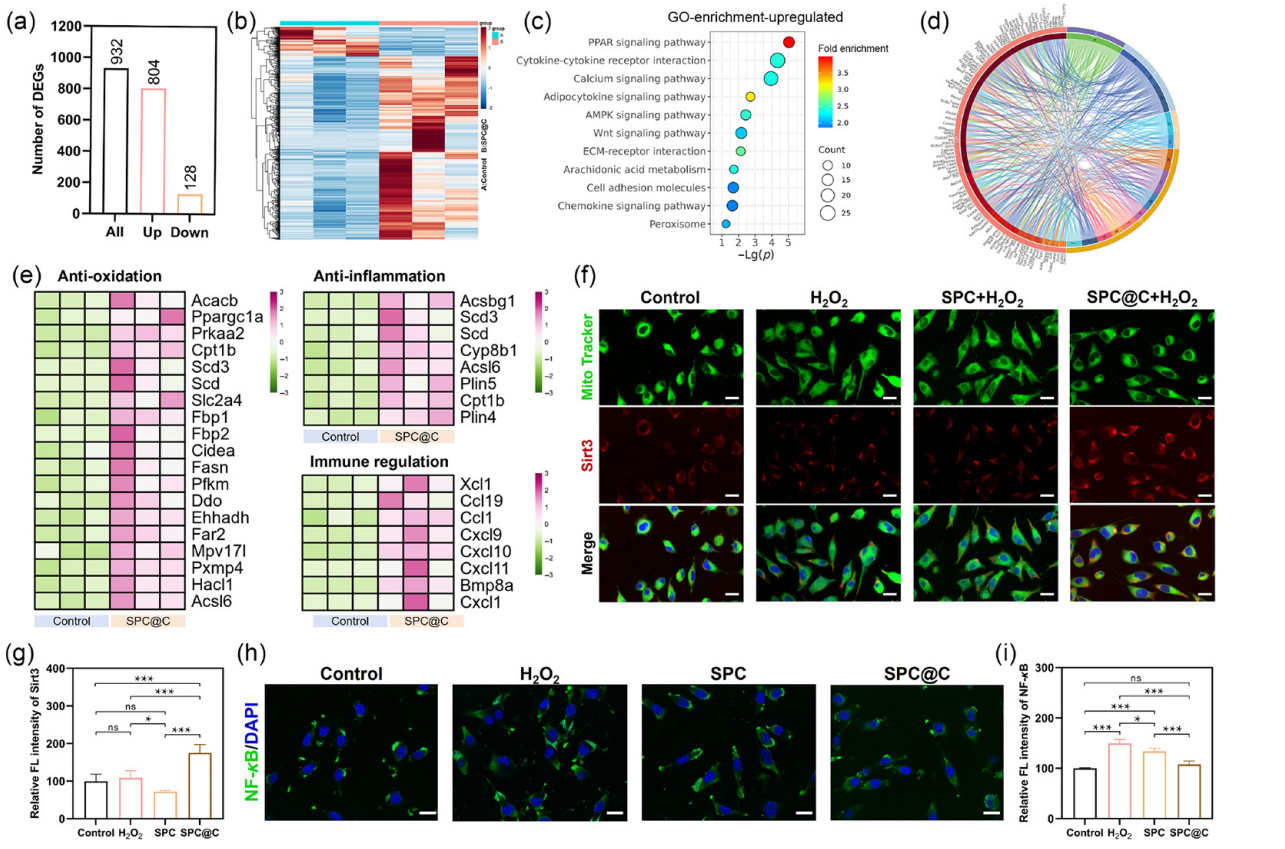

Figure 6 Transcriptomic profiling of burn wound tissues. (a) Differential gene expression: upregulated (red) and downregulated (yellow) genes ($|\log_2(\text{Fold change})| > 1$, adj. $p < 0.05$) ($n = 3$). (b) Heatmap of significantly DEGs. (c) KEGG pathway enrichment analysis of DEGs in SPC@C-treated wounds. (d) Circos plot visualizing enriched KEGG pathways. (e) Heatmap of genes related to anti-oxidant, anti-inflammation, and immune regulation in the comparison between the control group and the SPC@C group. (f) Immunofluorescence of Sirt3 in cells. Scale bars: 20 μm. (g) Quantified Sirt3 fluorescence intensity ($n = 5$). (h) NF-κB p65 immunofluorescence in cells. Scale bars: 20 μm. (i) Quantified NF-κB p65 fluorescence intensity ($n = 5$). Data was presented as mean ± SD. Statistical analysis was performed by one-way ANOVA. ns, no significance; $^*P < 0.05$ and $^{***}P < 0.001$.

3.7 The molecular mechanism underlying accelerated burn wound healing

Building on the demonstrated *in vitro* anti-inflammatory activity of SPC@C, we further validated its therapeutic efficacy using animal models *in vivo*. Immunohistochemical analysis revealed a significant reduction in IL-1β expression and a marked increase in IL-10 positivity in SPC@C-treated groups (Fig. 7(a)). Image J quantification revealed 52% ± 1.34% relative coverage area decrease in IL-1β and 61% ± 1.69% increase in IL-10 compared to control group (Figs. 7(b) and 7(c)). In addition, the expression of inflammation-related genes was evaluated by qPCR. As shown in Figs. 7(f) and 7(g), the mRNA expression of *Il-1β* was significantly decreased, while the *IL-10* was increased in the SPC@C group. These findings demonstrate the potent anti-inflammatory efficacy of SPC@C *in vivo*.

Given that sustained oxidative stress in burn wounds perpetuates inflammation, macrophages predominantly exhibit pro-inflammatory M1 phenotypes [55]. Immunofluorescence analysis revealed that SPC@C exerted a significant regulatory effect on macrophage polarization. On day 3, the fluorescence intensity of the M1 marker CD86 in SPC@C-treated wounds was significantly enhanced, while the M2 marker CD206 showed no significant change (Fig. 7(d)). Studies have indicated that an early active inflammatory response in the wound healing was conducive to the transition to the proliferative phase. However, persistent inflammation in the later stage hinders tissue repair [55]. On day 7, SPC@C treatment markedly increased CD206 fluorescence intensity while reducing CD86 signals (Fig. 7(d)). Quantitative analysis indicated that the CD206/CD86 ratio in the SPC@C group was 3.8 times higher than in the control group (Fig. 7(e)), indicating accelerated M1-to-M2 phenotypic conversion. These findings demonstrate that SPC@C treatment facilitates the critical transition from inflammatory to proliferative healing phases. The SPC@C patch plays a pivotal role in reprogramming macrophage responses during early inflammation resolution, thereby creating a regenerative microenvironment conducive to tissue repair.

To elucidate the underlying molecular mechanisms, we investigated the expression of Sirt3, a master regulator of antioxidant defense, in a rat burn model [56]. Notably, SPC@C-treated wound tissues exhibited enhanced Sirt3 immunofluorescence intensity alongside concomitant reduction in NF-κB p65 signal, compared to untreated burn controls (Figs. 7(h)–7(k)). Elevated Sirt3 expression activated downstream SOD2 [57], thereby enhancing cellular antioxidant capacity. Consistent with this pathway, *in vitro* analysis confirmed significantly intensified SOD2 fluorescence following SPC@C treatment compared with the control group (Fig. S12 in the ESM). qPCR analysis of animal tissues revealed upregulation of *Sirt3* gene expression (Fig. 7(l)), and downregulation of *NF-κB p65* gene

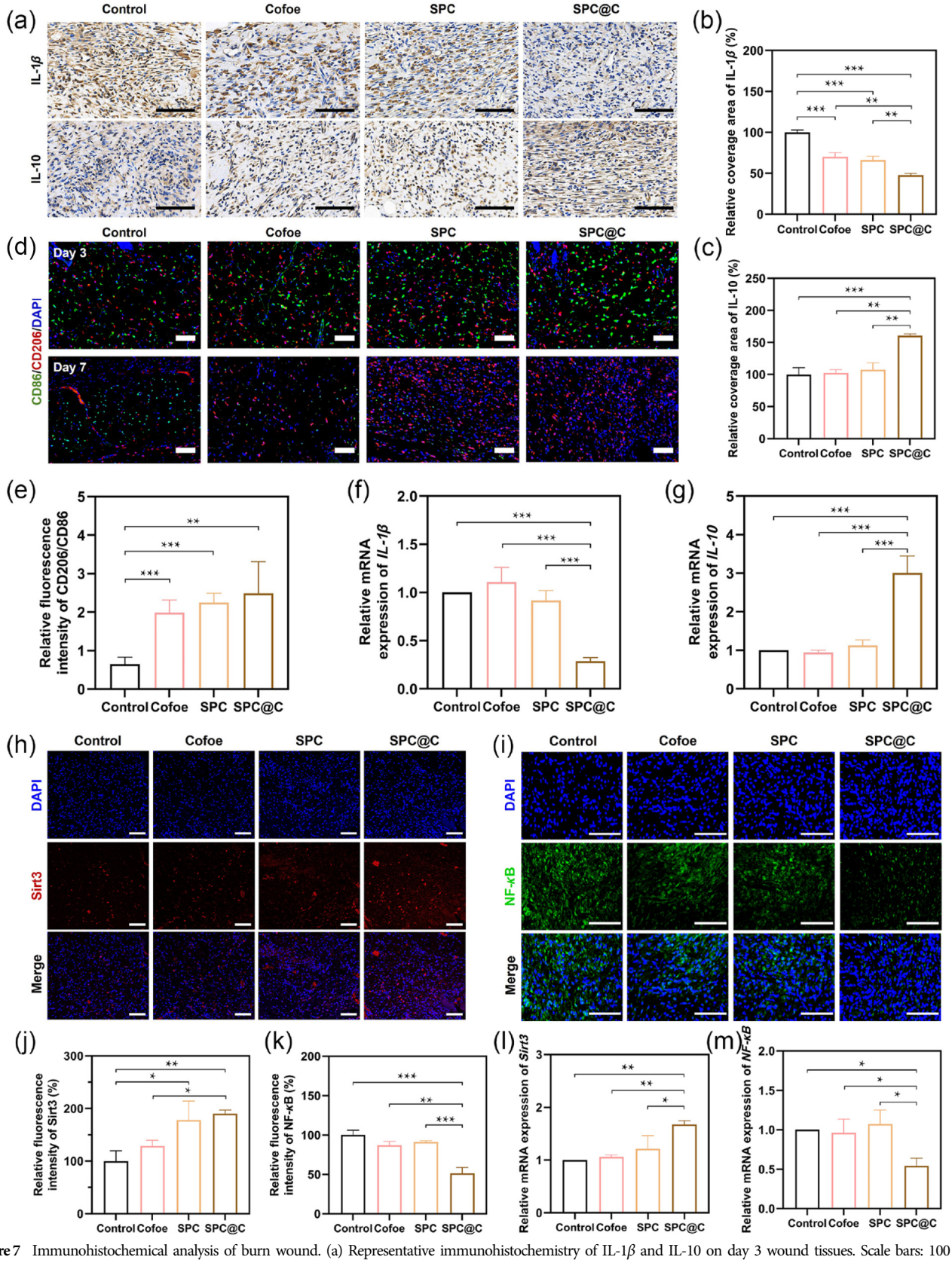

Figure 7 Immunohistochemical analysis of burn wound. (a) Representative immunohistochemistry of IL-1β and IL-10 on day 3 wound tissues. Scale bars: 100 μm. Quantified coverage area of (b) IL-1$\beta$and (c) IL-10 (n = 3). (d) Dual immunofluorescence staining of CD86 and CD206 macrophages in wounds at days 3 and 7. Scale bars: 100 μm. (e) CD206/CD86 fluorescence intensity ratio (n = 3). Relative mRNA expression of (f) *IL-1β* and (g) *IL-10* by qPCR (n = 3). Immunofluorescence of (h) Sirt3 and (i) NF-κB p65 in day 7 wounds. Scale bars: 100 μm. Quantified fluorescence intensity of (j) Sirt3 and (k) NF-κB p65 (n = 3). Relative mRNA expression of (l) *Sirt3* and (m) *NF-κB* by qPCR (n = 3). Data was presented as mean ± SD. Statistical analysis was performed by one-way ANOVA. *P < 0.05, **P < 0.01, and ***P < 0.001.

expression (Fig. 7(m)). These gene changes aligned with immunofluorescence characterization. Collectively, SPC@C synergistically attenuates oxidative stress and inflammation via the concerted action of activating the Sirt3/SOD2 antioxidant axis and suppression of NF-κB-mediated inflammatory signaling, ultimately promoting angiogenesis and tissue regeneration.

Impaired angiogenesis represents a pivotal determinant of dysfunctional wound repair during the proliferative phase [58]. To quantitatively evaluate this process, immunofluorescence analysis of CD31 vessels was systematically performed. As shown in Fig. S13 in the ESM, wounds treated with SPC@C exhibited substantially stronger CD31 fluorescence intensity compared to controls. Collagen deposition plays a pivotal role in the remodeling phase, facilitating skin repair and reinforcing tissue tensile strength [59]. Consequently, subcutaneous collagen deposition and reorganization serve as critical indicators of wound healing progression. To evaluate collagen remodeling following SPC@C patch treatment, we performed immunofluorescence staining for collagen alpha-1(I) chain (Col I) (Fig. S14 in the ESM). The treated groups exhibited significantly enhanced collagen deposition compared to controls, which showed only minimal accumulation. These findings collectively indicate that the SPC@C patch effectively modulates the inflammatory and proliferative phases to promote tissue remodeling in burn wounds, thereby facilitating comprehensive acceleration of burn tissue regeneration.

4 Conclusions

This study designed an SPC@C hydrogel patch with dual functionalities of ROS scavenging and immunomodulation. By integrating Cur-loaded BC nanoflowers, polyacrylamide, and sodium alginate, this patch constructed a multifunctional composite dressing system. The SPC@C patch absorbed excess wound exudate, inducing pore expansion within the polymeric network that facilitates controlled release of Cur nanoparticles. These nanoparticles effectively scavenged excessive ROS. Concomitantly, SPC@C orchestrated macrophage phenotypic polarization toward the M2 phenotype while downregulating pro-inflammatory cytokine expression (TNF-α and IL-1β). In Sprague-Dawley rat models with deep partial-thickness burns, the SPC@C patch significantly accelerated wound healing through inflammation attenuation, enhanced angiogenesis, and stimulated collagen deposition. RNA sequencing confirmed that SPC@C patch synergistically promoted tissue regeneration by activating the Sirt3/SOD2 antioxidant axis and inhibiting the NF-κB inflammatory pathway. This dual-functional design provides a promising candidate for clinical translation in burn wound management.

Electronic Supplementary Material: Supplementary material (the optical absorption properties of the nanoparticles measured by UV–vis spectrophotometry in the range of 300–600 nm; the micromorphology and elemental distribution of the materials observed using SEM coupled with EDS; and analyze of the surface chemical composition and elemental valence states by XPS (0–1200 eV)) is available in the online version of this article at https://doi.org/10.26599/NR.2026.94908787.

Data availability

All data needed to support the conclusions in the paper are presented in the manuscript and the Electronic Supplementary Material. Additional data related to this paper may be requested from the corresponding author upon request.

Acknowledgements

This work was supported by the National Natural Science Foundation of China (Nos. 82325012 and 82301043), Young Elite Scientist Support Program by CSA (No. 2024PYRC001), Young Talent Support Program of Shaanxi Province (No. 20240304), and the Postdoctoral Fellowship Program of CPSF (No. GZB20240994).

Declaration of competing interest

All the contributing authors report no conflict of interests in this work.

Author contribution statement

Q. B.: Conceptualization, writing – original draft. Y. Z. W.: Writing – review & editing. G. P. D.: Methodology, formal analysis. J. X. H.: Validation, resources. Y. B. J.: Data curation, methodology. Y. W.: Data curation. X. F. L.: Project administration. Y. F. W.: Methodology. L. W.: Supervision, visualization. J. T. G.: Visualization, funding acquisition. L. N. N.: Supervision, funding acquisition. All the authors have approved the final manuscript.

Informed consent

Not applicable.

Ethics statement

All experimental procedures involving animals were reviewed and approved by the Laboratory Animal Ethics Committee of the Air Force Military Medical University (Approval No.: 2024kq-054).

Use of AI statement

None.

References

[1] Jeschke, M. G.; van Baar, M. E.; Choudhry, M. A.; Chung, K. K.; Gibran, N. S.; Logsetty, S. Burn injury. *Nat. Rev. Dis. Primers* **2020**, *6*, 11.

[2] Lv, J. C.; Qiu, Y.; Liang, D. M.; Luo, H. C.; Wang, Z. G.; Liu, Y. W.; Zhou, J.; Li, Q. J.; Hong, R.; Li, K. et al. Unilateral surface-crystal-engineering induced dual-bionic Janus multifunctional wound dressing for infected burn wound healing. *Adv. Funct. Mater.* **2025**, *35*, 2503517.

[3] Song, J. H.; Gu, J. T.; Dang, G. P.; Wan, M. C.; Bai, Y. K.; Bai, Q.; Jiao, K.; Niu, L. N. DNA-collagen dressing for promoting scarless healing in early burn wound management. *Adv. Compos. Hybrid Mater.* **2025**, *8*, 212.

[4] Church, D.; Elsayed, S.; Reid, O.; Winston, B.; Lindsay, R. Burn wound infections. *Clin. Microbiol. Rev.* **2006**, *19*, 403–434.

[5] Wang, Y. W.; Beekman, J.; Hew, J.; Jackson, S.; Issler-Fisher, A. C.; Parungao, R.; Lajevardi, S. S.; Li, Z.; Maitz, P. K. M. Burn injury: Challenges and advances in burn wound healing, infection, pain and scarring. *Adv. Drug Deliv. Rev.* **2018**, *123*, 3–17.

[6] Lan, J. Z.; Shi, L. X.; Xiao, W. Y.; Zhang, X. B.; Wang, S. T. A rapid self-pumping organohydrogel dressing with hydrophilic fractal microchannels to promote burn wound healing. *Adv. Mater.* **2023**, *35*, 2301765.

[7] Wang, Y. X.; Wang, H. Y.; Lu, B. T.; Yu, K.; Xie, R. Q.; Lan, G. Q.;

Xie, J.; Hu, E. L.; Lu, F. A sandwich-like silk fibroin/polysaccharide composite dressing with continual biofluid draining for wound exudate management. *Int. J. Biol. Macromol.* **2023**, *253*, 127000.
[8] Cheng, H.; Li, C. J.; Jiang, Y. J.; Wang, B. J.; Wang, F. J.; Mao, Z. P.; Xu, H.; Wang, L.; Sui, X. F. Facile preparation of polysaccharide-based sponges and their potential application in wound dressing. *J. Mater. Chem. B* **2018**, *6*, 634–640.
[9] Hu, Y.; Yu, B. R.; Jia, Y. B.; Lei, M.; Li, Z. J.; Liu, H.; Huang, H. S.; Xu, F.; Li, J.; Wei, Z. Hyaluronate- and gelatin-based hydrogels encapsulating doxycycline as a wound dressing for burn injury therapy. *Acta Biomater.* **2023**, *164*, 151–158.
[10] Feng, F.; Zhao, Z. H.; Li, J. W.; Huang, Y. S.; Chen, W. C. Multifunctional dressings for wound exudate management. *Prog. Mater. Sci.* **2024**, *146*, 101328.
[11] Zeng, Q. K.; Qi, X. L.; Shi, G. Y.; Zhang, M.; Haick, H. Wound dressing: From nanomaterials to diagnostic dressings and healing evaluations. *ACS Nano* **2022**, *16*, 1708–1733.
[12] Liu, H. Z.; Sun, W. B.; Cai, W. H.; Luo, K. D.; Lu, C. X.; Jin, A. X.; Zhang, J. T.; Liu, Y. Y. Current status, challenges, and prospects of artificial intelligence applications in wound repair theranostics. *Theranostics* **2025**, *15*, 1662–1688.
[13] Goh, M.; Du, M.; Peng, W. R.; Saw, P. E.; Chen, Z. Y. Advancing burn wound treatment: Exploring hydrogel as a transdermal drug delivery system. *Drug Deliv.* **2024**, *31*, 2300945.
[14] Wang, Y.; Vizely, K.; Li, C. Y.; Shen, K. R.; Shakeri, A.; Khosravi, R.; Smith, J. R.; Alteza, E. A. I. I.; Zhao, Y. M.; Radisic, M. Biomaterials for immunomodulation in wound healing. *Regen. Biomater.* **2024**, *11*, rbae032.
[15] Zhao, X.; Xu, H. R.; Sun, Y. C.; Yang, Y. T.; Guo, B. L. Self-adaptive wound dressings for wound healing and repair. *Adv. Mater.*, in press, DOI: 10.1002/adma.202515854.
[16] Mehmood, S.; Ullah, I.; Hussain, Z.; Dawit, H.; Ullah, S.; Liu, X. Z.; Ahmed, W.; Xu, M. S.; Cao, Y.; Pei, R. J. Bioactive self-pumping Janus fibrous hydrogel dressings with aligned microneedle channels for chronic wound healing. *Adv. Funct. Mater.* **2026**, *36*, e04317.
[17] Wang, Y. B.; Ma, Q.; Zheng, B. N.; Xiong, W. X.; Miao, D. T.; Li, Y.; Huang, R. K.; Wang, H.; Wu, D. C. Electroactive dressing with selective sorption of exudate enables treatment of complicated wound. *Adv. Mater.* **2025**, *37*, 2413320.
[18] Zhao, M. J.; Kang, M. M.; Wang, J. R.; Yang, R. H.; Zhong, X. P.; Xie, Q. H.; Zhou, S. T.; Zhang, Z. J.; Zheng, J. D.; Zhang, Y. X. et al. Stem cell-derived nanovesicles embedded in dual-layered hydrogel for programmed ROS regulation and comprehensive tissue regeneration in burn wound healing. *Adv. Mater.* **2024**, *36*, 2401369.
[19] Deng, L. L.; Du, C. Z.; Song, P. Y.; Chen, T. Y.; Rui, S. L.; Armstrong, D. G.; Deng, W. Q. The role of oxidative stress and antioxidants in diabetic wound healing. *Oxid. Med. Cell. Longev.* **2021**, *2021*, 8852759.
[20] George, B.; Suchithra, T. V.; Bhatia, N. Burn injury induces elevated inflammatory traffic: The role of NF-κB. *Inflamm. Res.* **2021**, *70*, 51–65.
[21] Parihar, A.; Parihar, M. S.; Milner, S.; Bhat, S. Oxidative stress and anti-oxidative mobilization in burn injury. *Burns* **2008**, *34*, 6–17.
[22] Li, C. L.; Deng, C. S.; Wang, S. W.; Dong, X.; Dai, B.; Guo, W. D.; Guo, Q. Q.; Feng, Y. L.; Xu, H. D.; Song, X. Y. et al. A novel role for the ROS-ATM-Chk2 axis mediated metabolic and cell cycle reprogramming in the M1 macrophage polarization. *Redox Biol.* **2024**, *70*, 103059.
[23] Rendra, E.; Riabov, V.; Mossel, D. M.; Sevastyanova, T.; Harmsen, M. C.; Kzhyshkowska, J. Reactive oxygen species (ROS) in macrophage activation and function in diabetes. *Immunobiology* **2019**, *224*, 242–253.
[24] Forrester, S. J.; Kikuchi, D. S.; Hernandes, M. S.; Xu, Q.; Griendling, K. K. Reactive oxygen species in metabolic and inflammatory signaling. *Circ. Res.* **2018**, *122*, 877–902.
[25] Joorabloo, A.; Liu, T. Q. Recent advances in reactive oxygen species scavenging nanomaterials for wound healing. *Exploration* **2024**, *4*, 20230066.
[26] Yuan, R. Y. K.; Li, Y. Q.; Han, S.; Chen, X. X.; Chen, J. Q.; He, J.; Gao, H. W.; Yang, Y.; Yang, S. L.; Yang, Y. Fe-curcumin nanozyme-mediated reactive oxygen species scavenging and anti-inflammation for acute lung injury. *ACS Cent. Sci.* **2022**, *8*, 10–21.
[27] Li, D. Y.; Zhang, C. J.; Gao, Z. S.; Xia, N.; Wu, C.; Liu, C.; Tian, H.; Mei, X. F. Curcumin-loaded macrophage-derived exosomes effectively improve wound healing. *Mol. Pharm.* **2023**, *20*, 4453–4467.
[28] Fu, J. J.; Mei, S. Y.; Zhang, Q. C.; Fu, X. Y.; Zhong, J. C.; Deng, J.; Zhang, Q. B.; Bai, X. Y.; He, F. Y.; Wu, J. X. et al. Multifunctional hydrogel dressing based on glycosylated collagen-curcumin nanoparticles effectively accelerates wound healing. *Adv. Healthc. Mater.* **2026**, *15*, e00554.
[29] Wu, J.; Wang, W. T.; Shen, J.; Zhou, N. L.; Li, Y. Y.; Tang, B. Z.; Zhang, M. A thermosensitive hydrogel with efficient NIR photothermal conversion as injectable wound dressing for accelerating skin wound healing. *Adv. Funct. Mater.* **2024**, *34*, 2312374.
[30] Tong, Q. L.; Yi, Z.; Ma, L.; Tan, Y. F.; Liu, D. N.; Cao, X. Y.; Ma, X. M.; Li, X. D. Microenvironment-responsive antibacterial, anti-inflammatory, and antioxidant Pickering emulsion stabilized by curcumin-loaded tea polyphenol particles for accelerating infected wound healing. *ACS Appl. Mater. Interfaces* **2024**, *16*, 44467–44484.
[31] Wang, X.; Huo, H. L.; Cao, L.; Zhong, Y. M.; Gong, J.; Lin, Z. D.; Xie, X. B.; Bao, Z.; Zhang, P. Curcumin-release antibacterial dressings with antioxidation and anti-inflammatory function for diabetic wound healing and glucose monitoring. *J. Control. Release* **2025**, *378*, 153–169.
[32] Huang, R. Y.; Sun, W. J.; Li, W. Z.; Hu, R.; Meng, R.; Peng, Z.; Yang, R. B.; Huang, T. Y.; Du, J. H.; Shang, L. R. et al. Immunomodulatory hydrogel patches loaded with curcumin and tannic acid assembled nanoparticles for radiation dermatitis repair and radioprotection. *Chem. Eng. J.* **2024**, *500*, 156869.
[33] Wang, F.; He, W. Q.; Dai, B.; Zhang, X. J.; Wen, Y. Q. Recent advances in asymmetric wettability dressings for wound exudate management. *Research* **2025**, *8*, 0591.
[34] Wu, S. J.; Zhao, X. H. Bioadhesive technology platforms. *Chem. Rev.* **2023**, *123*, 14084–14118.
[35] Yuk, H.; Varela, C. E.; Nabzdyk, C. S.; Mao, X. Y.; Padera, R. F.; Roche, E. T.; Zhao, X. H. Dry double-sided tape for adhesion of wet tissues and devices. *Nature* **2019**, *575*, 169–174.
[36] Wang, C. H.; Chen, X. Y.; Wang, L.; Makihata, M.; Liu, H. C.; Zhou, T.; Zhao, X. H. Bioadhesive ultrasound for long-term continuous imaging of diverse organs. *Science* **2022**, *377*, 517–523.
[37] Li, J.; Celiz, A. D.; Yang, J.; Yang, Q.; Wamala, I.; Whyte, W.; Seo, B. R.; Vasilyev, N. V.; Vlassak, J. J.; Suo, Z. et al. Tough adhesives for diverse wet surfaces. *Science* **2017**, *357*, 378–381.
[38] Jiang, Y. N.; Zhang, X.; Zhang, W.; Wang, M. H.; Yan, L. W.; Wang, K. F.; Han, L.; Lu, X. Infant skin friendly adhesive hydrogel patch activated at body temperature for bioelectronics securing and diabetic wound healing. *ACS Nano* **2022**, *16*, 8662–8676.
[39] An, H.; Zhang, M.; Zhou, L. P.; Huang, Z.; Duan, Y. C.; Wang, C.; Gu, Z.; Zhang, P. X.; Wen, Y. Q. Anti-dehydration and rapid trigger-detachable multifunctional hydrogels promote scarless therapeutics of deep burn. *Adv. Funct. Mater.* **2023**, *33*, 2211182.
[40] Tang, Y.; Gong, G. D.; He, X. L.; Dai, M. Y.; Chen, M.; Wang, B.; Wang, Y. J.; Wang, X. L.; Guo, J. L. Multifunctional dual cross-linked bioadhesive patch with low immunogenic response and wet tissues adhesion. *Adv. Healthc. Mater.* **2023**, *12*, 2201578.
[41] Camargo, L. L.; Rios, F. J.; Montezano, A. C.; Touyz, R. M. Reactive oxygen species in hypertension. *Nat. Rev. Cardiol.* **2025**, *22*, 20–37.
[42] Sies, H.; Jones, D. P. Reactive oxygen species (ROS) as pleiotropic

physiological signalling agents. *Nat. Rev. Mol. Cell Biol.* **2020**, *21*, 363–383.
[43] Nathan, C.; Cunningham-Bussel, A. Beyond oxidative stress: An immunologist's guide to reactive oxygen species. *Nat. Rev. Immunol.* **2013**, *13*, 349–361.
[44] Ding, J.; Mei, S. S.; Wang, K. L.; Cheng, W.; Sun, S.; Ni, Z. X.; Wang, X. Q.; Yu, C. Q. Curcumin modulates oxidative stress to inhibit pyroptosis and improve the inflammatory microenvironment to treat endometriosis. *Genes Dis.* **2024**, *11*, 101053.
[45] Chen, Y.; Wang, J. J.; Jing, Z. H.; Ordovas, J. M.; Wang, J.; Shen, L. R. Anti-fatigue and anti-oxidant effects of curcumin supplementation in exhaustive swimming mice via Nrf2/Keap1 signal pathway. *Curr. Res. Food Sci.* **2022**, *5*, 1148–1157.
[46] Sena, L. A.; Chandel, N. S. Physiological roles of mitochondrial reactive oxygen species. *Mol. Cell* **2012**, *48*, 158–167.
[47] Jiang, T. Y.; Xiao, Y.; Zhou, J. F.; Luo, Z. P.; Yu, L.; Liao, Q. C.; Liu, S. Q.; Qi, X. Y.; Zhang, H.; Hou, M. L. et al. Arbutin alleviates fatty liver by inhibiting ferroptosis via FTO/SLC7A11 pathway. *Redox Biol.* **2023**, *68*, 102963.
[48] Casey, A. M.; Ryan, D. G.; Prag, H. A.; Chowdhury, S. R.; Marques, E.; Turner, K.; Gruszczyk, A. V.; Yang, M.; Wolf, D. M.; Miljkovic, J. L. et al. Pro-inflammatory macrophages produce mitochondria-derived superoxide by reverse electron transport at complex I that regulates IL-1β release during NLRP3 inflammasome activation. *Nat. Metab.* **2025**, *7*, 493–507.
[49] Guan, F.; Wang, R. X.; Yi, Z. J.; Luo, P.; Liu, W. Y.; Xie, Y.; Liu, Z. Q.; Xia, Z. W.; Zhang, H.; Cheng, Q. Tissue macrophages: Origin, heterogenity, biological functions, diseases and therapeutic targets. *Signal Transduct. Target. Ther.* **2025**, *10*, 93.
[50] Qian, Y. N.; Ding, J. Y.; Zhao, R.; Song, Y.; Yoo, J.; Moon, H.; Koo, S.; Kim, J. S.; Shen, J. L. Intrinsic immunomodulatory hydrogels for chronic inflammation. *Chem. Soc. Rev.* **2025**, *54*, 33–61.
[51] Lawrence, T.; Natoli, G. Transcriptional regulation of macrophage polarization: Enabling diversity with identity. *Nat. Rev. Immunol.* **2011**, *11*, 750–761.
[52] Sies, H.; Mailloux, R. J.; Jakob, U. Fundamentals of redox regulation in biology. *Nat. Rev. Mol. Cell Biol.* **2024**, *25*, 701–719.
[53] Sies, H.; Belousov, V. V.; Chandel, N. S.; Davies, M. J.; Jones, D. P.; Mann, G. E.; Murphy, M. P.; Yamamoto, M.; Winterbourn, C. Defining roles of specific reactive oxygen species (ROS) in cell biology and physiology. *Nat. Rev. Mol. Cell Biol.* **2022**, *23*, 499–515.
[54] Peng, F.; Liao, M. R.; Jin, W. K.; Liu, W.; Li, Z. X.; Fan, Z. C.; Zou, L.; Chen, S. W.; Zhu, L. J.; Zhao, Q. et al. 2-APQC, a small-molecule activator of Sirtuin-3 (SIRT3), alleviates myocardial hypertrophy and fibrosis by regulating mitochondrial homeostasis. *Signal Transduct. Target. Ther.* **2024**, *9*, 133.
[55] Chen, C.; Liu, T. F.; Tang, Y. Y.; Luo, G. X.; Liang, G. P.; He, W. F. Epigenetic regulation of macrophage polarization in wound healing. *Burns Trauma* **2023**, *11*, tkac057.
[56] Mao, A. M.; Fu, Y. J.; Zhang, M. H.; Wu, J. N.; Wu, M. J. Phenotypic screening identified polydatin alleviating cartilage degeneration by modulating SIRT3-dependent mitochondrial dysfunction. *Phytomedicine* **2025**, *144*, 156948.
[57] Lin, L.; Sun, B. W.; Hu, Y. L.; Yang, W. Q.; Li, J.; Wang, D. Y.; Zhang, L.; Lu, M. K.; Li, Y.; Li, Y. L. et al. Rhynchophylline as an agonist of sirtuin 3 ameliorates endothelial dysfunction via antagonizing mitochondrial damage of endothelial progenitor cells. *Br. J. Pharmacol.* **2025**, *182*, 3476–3502.
[58] Rodrigues, M.; Kosaric, N.; Bonham, C. A.; Gurtner, G. C. Wound healing: A cellular perspective. *Physiol. Rev.* **2019**, *99*, 665–706.
[59] Peña, O. A.; Martin, P. Cellular and molecular mechanisms of skin wound healing. *Nat. Rev. Mol. Cell Biol.* **2024**, *25*, 599–616.